# Aluminum Nanowire Arrays via Directed Assembly

Nathan T. Nesbitt,* Juan M. Merlo, Aaron H. Rose, Yitzi M. Calm, Krzysztof Kempa, Michael J. Burns, and Michael J. Naughton*

Department of Physics, Boston College, 140 Commonwealth Avenue, Chestnut Hill, Massachusetts 02467, United States

Ⓢ Supporting Information

ABSTRACT: Freestanding and vertically-oriented metal nanowire arrays have potential utility in a number of applications, but presently lack a route to fabrication. Template-based techniques, such as electrodeposition into lithographically defined nanopore arrays, have produced well-ordered nanowire arrays with a maximum pitch of about 2 μm; such nanowires, however, tend to cluster due to local attractive forces. Here, we modify this template fabrication method to produce well-ordered, vertically-oriented, freestanding Al nanowire arrays, etched from an underlying Al substrate, with highly tunable pitch. In addition, optical measurements demonstrated that the nanowires support the propagation of surface plasmon polaritons.

KEYWORDS: Metal nanowires, anodized aluminum oxide (AAO), plasmonics
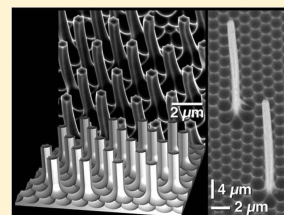
Vertically-oriented, lithographically-ordered, metal nanowire arrays have potential utility as capacitors,[1] high surface area electrodes,[2] electrochemical biosensors,[3] optical nanoscopes,[4,5] rectennas,[6,7] and solar cells.[8−12] In many of these applications, the nanowires are coated with materials to produce core−shell or nanocoax structures,[13] which, for many deposition processes, requires the nanowires to be freestanding to accomplish a homogeneous coating.

Currently, only a limited range of nanowire heights and array pitches can be produced in ordered arrays using metallic materials. Chemical vapor deposition, a method of nanowire fabrication with tunable height and pitch, produces metal nanowires in only disordered arrays (Figure 1a)[14,15] or carbon nanofibers having low electrical conductivity (~10^4 S/m,[16,17] three decades lower than good metals[18]) (Figure 1b). Electroplating metals in anodized aluminum oxide (AAO) template nanopores produces highly conductive and ordered arrays (Figure 1c),[9,19−22] but a maximum pitch of 2 μm[9,20] typically causes the nanowires to cluster together due to local attractive forces.[23,24] As greater tunability of nanowire height and pitch could be advantageous for the aforementioned applications, we have modified the preparation of AAO templates to produce highly ordered and freestanding aluminum nanowire arrays (Figure 1d). This process etches the nanowires from the underlying substrate at lithographically defined locations, providing high tunability of the array geometry. Additionally, the process is amenable to low-cost, large-scale production because it is solution based, roll-to-roll compatible,[9,25] operates at atmospheric pressure with temperatures between 0 and 60 °C, and uses Al, an earth abundant[26] and inexpensive metal.

An AAO template consists of an array of pores passing through the thickness of an oxidized aluminum film. The oxide is developed by anodizing the Al, with pores formed during anodization due to a positive-feedback process. Well-ordered arrays can be obtained by prepatterning the Al surface with an
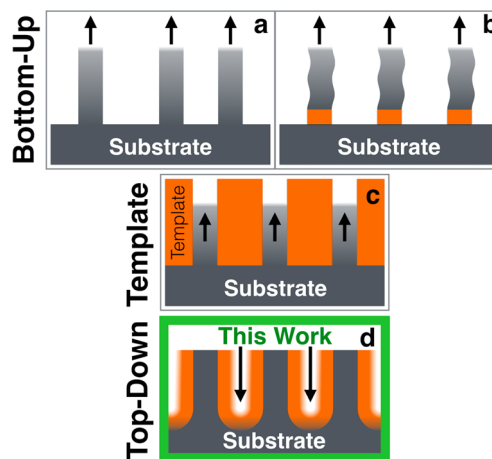

Figure 1. Methods of fabricating metal nanowire arrays. (a) Chemical vapor deposition (CVD) of Ni:[14,15] a bottom-up process that produces vertically-oriented nanowires with irregular spacing between them. (b) CVD of carbon nanofibers: a bottom-up process that produces disordered nanowires with poor conductivity relative to good metals;[16−18] orange rectangles represent particles the nanofibers nucleate on. (c) Electrodeposition of metal nanowires in templates:[9,19−22] a template-based method that produces metal nanowires in an ordered array. Existing templates, such as porous AAO, have limited pitch, which causes these wires to bundle; orange rectangles represent a porous template. (d) Al nanowire arrays via directed assembly: a top-down process that produces lithographically-ordered, vertically-oriented, freestanding metal nanowire arrays—possibly the first top-down method of metal nanowire fabrication; orange layer represents AAO.
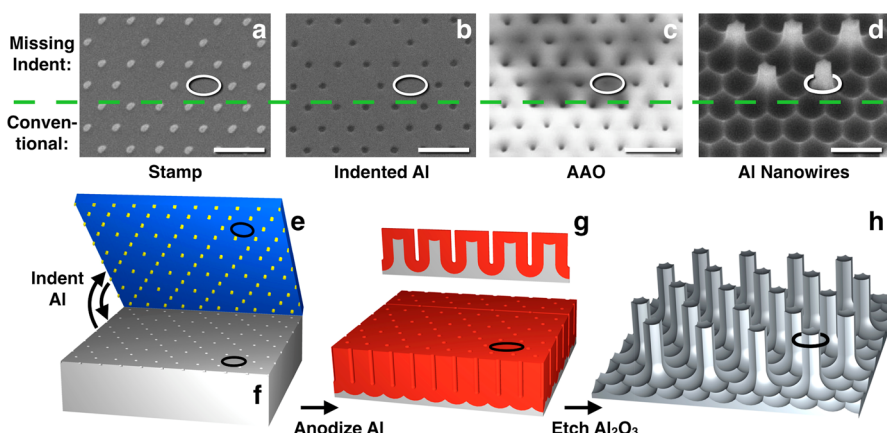
Figure 2. Fabrication process of Al nanowires, with representative SEM data of neighboring regions on the sample showing each step on top, and corresponding cartoons on bottom. (a) SEM of Ni stamp used to indent the Al, (b) SEM of indented Al surface, (c) SEM of AAO template surface, (d) SEM of Al nanowires, (e) cartoon of Ni stamp, (f) cartoon of the imprinted Al surface, (g) cartoon of the AAO template with missing pores with a cross-section of the template where Al nanowires are embedded, and (h) the Al nanowires after etching away the AAO. For parts a−d, above the dashed green line there is a periodic array of missing Ni posts in the stamp, translating into Al nanowires on the sample; below this line depicts a conventional AAO process with no posts missing from the stamp. Scale bars 2 μm.

ordered array of indents, steering pore nucleation at the indent sites,[27] as discussed in a recent review article.[28]

In our approach, fabrication of an Al nanowire requires a defect in the form of an intentional lack of an indent in the Al surface, which blocks the formation of a pore when anodizing the Al to produce an AAO template. Scanning electron microscope (SEM) images and associated schematics in Figure 2 demonstrate this process. A stamp composed of an array of Ni posts, with some posts missing from the array to produce directed defects (Figure 2a), is pressed against an Al film to create indents in the Al (Figure 2b). When the film is subsequently anodized, pores preferentially form at the indents, while the Al below the missing indents is protected from oxidation. This process yields Al nanowires embedded in the AAO template at the missing indent sites (Figure 2c). Selective postetching of the aluminum oxide leaves freestanding Al nanowires (Figure 2d). The locations of such nanowires can be lithographically controlled by the placement of the missing posts in the stamp. As such, the nanowires can be as far from each other as desired, or as close to each other as separated by one anodized pore (e.g., 2.4 μm center-to-center in Figure 5a). We found that for stamps with Ni posts of variable diameter, from 200 to 700 nm, there was a maximum Ni post diameter of approximately 400 nm that would produce an AAO template with embedded Al nanowires (Figure S1). Further details are provided in the Supporting Information.

To fabricate the Al nanowire arrays in Figures 3 and 5, we used a hexagonal array of Ni posts (∼400 nm diameter and height, 1.2 μm pitch), fabricated via electron beam lithography on a Ni-coated-glass surface, to imprint the aluminum. From this underlying hexagonal matrix, we fabricated both hexagonal (Figures 3a−c) and square (Figures 3d−f) arrays of nanowires by proper placement of missing posts in the stamp. Geometrically, an aluminum nanowire is the result of subtracting a cylinder with a hemispherical base (i.e., the pore and surrounding oxide) from the bulk aluminum at the site of each indent. For a hexagonal array of indents, each missing indent is surrounded by six indents, which ultimately produces Al nanowires with a hexagonal cross-section (Figure 3, parts b and e). Other lattice configurations of indents have been demonstrated to produce AAO templates, such as a square
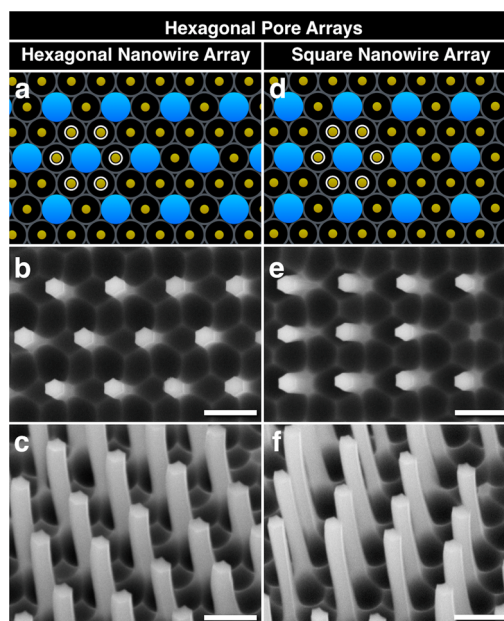

Figure 3. Diagram and SEMs demonstrating how the same underlying matrix (a hexagonal array of pores) can produce different lattice geometries of nanowires (hexagonal and square arrays). (a, d) Blue circles and yellow dots represent sites of nanowires and pores, respectively; circled yellow dots emphasize that all the nearest neighbors of a nanowire are pores, which causes the nanowires to have a hexagonal cross-section. (b, e) SEMs of resulting Al nanowire arrays in a (left) hexagonal lattice and (right) square lattice, tilt 0°. (c, f) SEMs of same region with tilt 30°. Scale bars 2 μm.

array,[9] and may also produce Al nanowires; we expect a square array of indents would produce Al nanowires with square cross-section.

To explain the growth mechanism of the nanowires, we compare our results to previous reports of imprinting a hexagonal array of indents into Al and leaving out indents at certain sites in the hexagonal lattice. In a study using an aqueous oxalic acid solution,[29] the lack of an indent had little impact on the pore formation and subsequent AAO template—pores formed at the sites of missing indents nearly as well as at
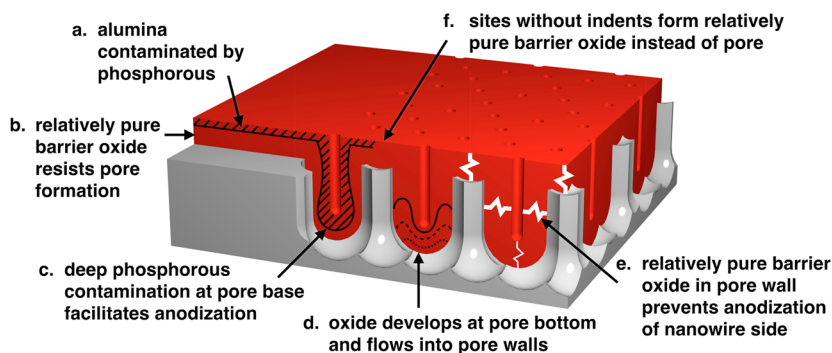
Figure 4. Mechanism of Al nanowire growth. (a) Studies have shown phosphorus from the electrolyte to penetrate into the alumina, (b) with a layer of relatively pure alumina adjacent to the oxide/metal interface (barrier oxide);[31] we propose this pure layer may resist deformation into a pore at sites where the Al surface was not indented. (c) Studies have shown the phosphorus to penetrate deeper into the oxide at the pore base than along the pore walls.[36] (d) On the basis of a separate study, this may result from plastic flow of relatively pure alumina from the metal/oxide interface at the pore bottom up into the pore walls.[34] (e) This relatively pure alumina is thought to resist ion flow,[31] which may protect the Al nanowires from anodization through the pore wall. (f) Sites on the Al surface that are not indented, but surrounded by indents, produce Al nanowires, as demonstrated in this study.

sites with indents. In a study using an aqueous phosphoric acid solution,[30] a site with a missing indent produced a pore with a relatively small radius and caused adjacent pores to have diamond shaped cross sections, rather than the typical circular shape. In our study, using citric acid with very dilute phosphoric acid in a solution of half deionized water and half ethylene glycol (EG), a missing indent successfully prevented the formation of a pore.

The variations in the reports above, from minor impact on pore formation, to producing only a small pore, to fully blocking pore formation, track with several other trends in AAO fabrication. For example, a missing indent becomes less likely to form a pore as anodization voltage or pitch is increased.[29,30] Also, different electrolyte anions penetrate different percentages of the barrier layer oxide at the pore base,[31] and missing indents are less likely to form pores as this penetration depth decreases (see Supporting Information, Table S1, for details).

To explain how these trends impact pore formation we consider the flow model for AAO growth, in which mechanical instabilities in the oxide cause pore nucleation. Reports supporting this model[28,32−36] have found pore nucleation to result from buckling of the oxide film, forming walls around pores,[36] initiated during anodization when the applied potential was high enough for electrostriction of the oxide to overcome the oxide surface tension. Since anions contaminating the oxide near the electrolyte/oxide interface modify the oxide's mechanical properties, such as its surface tension[33,36] and elasticity,[37] the type and concentration of anions in the oxide determines the voltage at which pores nucleate. Such contamination by phosphorus anions into the oxide is depicted in Figure 4a. We propose that the low oxide contamination during anodization in phosphoric acid, compared to oxalic acid,[31] may be what limits the formation of a pore at a missing indent; the thick layer of relatively pure alumina may resist mechanical deformation into a pore during anodization (Figure 4b). Because of limited studies on citric acid anodization, the role of these anions is unclear; however, the model we propose would suggest that citric acid anions have limited penetration into the oxide.

This flow model also offers an explanation for why the Al nanowires do not anodize through the sidewall of the AAO pores. In a recent study of the distribution of elements within the alumina of a pore grown in phosphoric acid,[36] the pore wall was found to have less penetration of phosphorus anions than the pore base (Figure 4c). A separate study, using a tungsten tracer layer in the Al substrate to track the flow of oxide in the pore during anodization,[34] elucidates this result; they found that oxide was generated at the metal/oxide interface at the pore bottom, and then flowed up and out into the sidewalls of the pore, as depicted in Figure 4d. The expected high resistance to electronic and ionic flow[31] of the relatively pure oxide in the pore sidewalls and above the nanowires is highlighted in Figure 4e.

The Al nanowires were observed to have attributes desirable for technological applications. For example, the process that produces the nanowires yields a hexagonal cross-section with sharp edges and smooth, concave surfaces, including a 6-pointed crown shape. These features are evident in the SEM images in Figure 5. The crown points (Figure 5b) have radii of curvature ∼10 nm (Figure 5c). In addition to such small pitch arrays, we can also fabricate arrays with pitch over 10 μm, and with wire height to, e.g., 20 μm (Figure 5d). Such sharp edges and smooth surfaces may be of relevance for photonic and plasmonic applications,[38,39] such as electric field enhancement. The strong secondary electron signal at the nanowire edges, relative to that at the faces, in Figure 5a, is more probable than not evidence of such enhancement—the alternative explanation being charging due to an anomalously thick native oxide at the edges. Additionally, as the nanowires' purity is determined by that of the starting Al foil/substrate, these wires are 99.9995% Al. Because of a low bulk oxide content, surface plasmon resonances (SPRs) on the nanowires should have high light scattering efficiency—advantageous for certain plasmonic devices.[40] Panchromatic cathodoluminescence images of the nanowires (see Supporting Information, Figure S3) show these edges to be dark for measurements at normal incidence, but not for measurements with sample tilt of 30°—potential evidence of strong light scattering at the edges.

Although Al was the first metal whose plasmonic properties were studied in depth,[41] it has only recently been investigated for applications in nanostructured plasmonic devices.[40,42,43] This is a result of fabrication challenges for Al nanostructures[42,43] and the location of the Al SPR cutoff frequency in the deep UV;[44] most plasmonics research has focused on visible light manipulation. Noble metals such as Au and Ag have SPR
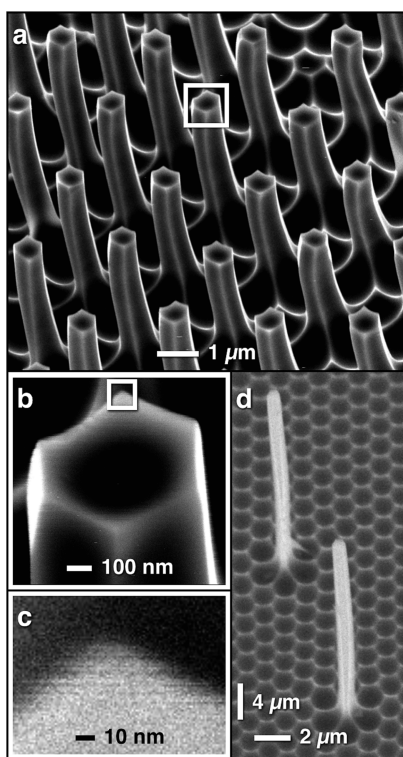
Figure 5. SEMs demonstrating attributes of the Al nanowires. (a) High contrast SEM of Al nanowires demonstrates electric field enhancement at the nanowire edges and corners. (b, c) SEMs show the radius of curvature of the nanowire corner to be ~10 nm. (d) SEM of Al nanowires with large height and pitch demonstrates tunability of Al nanowire array geometry. Tilt 30°.

Figure 6. Optical and AFM measurements of an Al nanowire on a glass slide and illuminated by a laser spot of wavelength 660 nm; laser polarization is along the wire axis to excite longitudinal SPP modes. (a) Composite NSOM and AFM signal:[49] figure topography shows NSOM signal, i.e., near-field optical intensity; color scale shows height of Al nanowire (red and yellow) and glass surface (blue), as measured by AFM. A yellow streak running lengthwise along the wire in the red region shows evidence of a ridge along the nanowire. White arrows highlight antinodes of standing waves on this ridge, formed by forward and backward propagating SPPs, which are created by the laser spot and reflection off the nanowire tip, respectively. (b, top) Black solid line shows line-cut of near-field optical intensity (NSOM) along dashed line in part a, demonstrating a standing wave of 550 nm wavelength in superposition with an exponentially decreasing intensity with increasing distance from the laser spot; red dashed line shows exponential fit that measures the standing-SPP decay length to be ~1 μm. (b, bottom) ΔI, the near-field optical intensity minus the exponential fit, shows the standing wave with greater clarity; gray arrows spaced by 550 nm highlight antinodes. (c) Far-field images of the Al nanowire under the laser spot show increasing light scattering from the Al nanowire tip with decreasing distance between the laser spot and the tip, likely due to SPPs propagating from the laser spot and scattering off the nanowire tip into photons; scale bar 2 μm.

cutoff frequencies in the visible and near-UV,[40,45,46] respectively, which have made them materials of choice for plasmonic device development. Recent studies, however, have demonstrated SPR modes on Al disks and rectangles,[42,47] as well as improved performance in sensors and photovoltaics using arrays of such structures.[11,48]

To elucidate the plasmonic properties of the Al nanowires, measurements with a near-field scanning optical microscope (NSOM), an atomic force microscope (AFM), and a conventional optical microscope (imaged onto a CCD) were taken of an isolated nanowire lying flat on glass and illuminated by a laser spot with 660 nm wavelength (see Supporting Information, Figure S4). The nanowire height (AFM signal), encoded as the color scale in Figure 6a, shows lengthwise ridges running along the nanowire; the electric field intensity (NSOM signal), encoded as the topography of Figure 6a, shows evidence of surface plasmon polaritons (SPPs) propagating from the laser spot along the nanowire length at the ridges. The apparent AFM signal modulations along the nanowire length are the artifact of the shading effect from the overlying NSOM pattern. A line-cut of the NSOM signal along a ridge (Figure 6b) shows the SPP standing wave pattern with wavelength of ~550 nm. Simulations (not shown) predict the SPP wavelength to be 600 nm for an Al nanowire coated by 3−5 nm of aluminum oxide and illuminated by 660 nm radiation. Images taken with the conventional optical microscope (Figure 6c) show light scattering from the nanowire tip with increasing intensity as the tip is moved closer to the laser spot, providing evidence that light is coupled from the laser spot to SPPs on the nanowire, and scattered into photons at the nanowire tip.
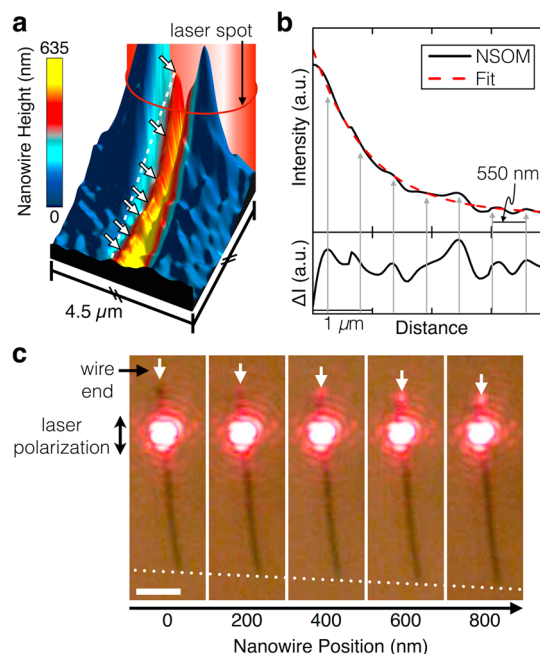
The large wavelength of the standing wave pattern in Figure 6b (approaching the SPP wavelength) results from the large (compared to SPP wavelength) circumference of the wire. This causes the backscattered SPP waves to have small axial components of their wave vectors, and therefore the resulting standing wave along the wire has its wave vector dominated by the incoming wave. This also explains the rapid decay of the standing wave pattern (with exponential decay range of ~1 μm), as shown in Figure 6b; due to the large wire circumference, a significant fraction of the SPP scatters away from the propagation channel along the wire ridge. This, with increasing distance away from the excitation point, effectively depletes the ridge propagation channel of plasmon waves. This evidence of SPPs supported on and guided along an Al nanowire demonstrates the potential efficacy of these Al nanowires for plasmonic device applications, such as a waveguide for light.

In conclusion, we have demonstrated a tunable process for template-free fabrication of vertically-oriented, spatially-ordered, freestanding aluminum nanowire arrays with lateral spacing unobtainable by existing metal nanowire fabrication processes. The arrays' high conductivity and unique spatial dimensions have potential utility in electrical, electrochemical, photonic and photovoltaic applications. Additionally, the nanowire topography has sharp edges and smooth surfaces that may be favorable for electric field enhancement and plasmonic applications. Finally, the process shows promise to be scalable for low-cost manufacturing of large surface area (m^2) devices.

■ ASSOCIATED CONTENT

Ⓢ Supporting Information

The Supporting Information is available free of charge on the ACS Publications website at DOI: 10.1021/acs.nano-lett.5b02408.

> Further details on fabrication procedures, the influence of indent diameter on pore formation, cathodolumines-cence measurements, and the NSOM setup (PDF)

■ AUTHOR INFORMATION

Corresponding Authors

*(N.T.N.) E-mail: nathan.nesbitt@gmail.com.
*(M.J.N.) E-mail: naughton@bc.edu.

■ REFERENCES

(1) Banerjee, P.; Perez, I.; Henn-Lecordier, L.; Lee, S. B.; Rubloff, G. W. *Nat. Nanotechnol.* **2009**, *4*, 292−296.

(2) Mckone, J. R.; Warren, E. L.; Bierman, M. J.; Boettcher, S. W.; Brunschwig, B. S.; Lewis, N. S.; Gray, H. B. *Energy Environ. Sci.* **2011**, *4*, 3573−3583.

(3) Rizal, B.; Archibald, M. M.; Connolly, T.; Shepard, S.; Burns, M. J.; Chiles, T. C.; Naughton, M. J. *Anal. Chem.* **2013**, *85*, 10040−10044.

(4) Rose, A. H.; Wirth, B. M.; Hatem, R. E.; Rashed Ahmed, A. P.; Burns, M. J.; Naughton, M. J.; Kempa, K. *Opt. Express* **2014**, *22*, 5228−5233.

(5) Shvets, G.; Trendafilov, S.; Pendry, J. B.; Sarychev, A. *Phys. Rev. Lett.* **2007**, *99*, 053903.

(6) Bailey, R. L. *J. Eng. Power* **1972**, *94*, 73−77.

(7) Wang, Y.; Kempa, K.; Kimball, B.; Carlson, J. B.; Benham, G.; Li, W. Z.; Kempa, T.; Rybczynski, J.; Herczynski, A.; Ren, Z. F. *Appl. Phys. Lett.* **2004**, *85*, 2607−2609.

(8) Camacho, R. E.; Morgan, A. R.; Flores, M. C.; McLeod, T. A.; Kumsomboone, V. S.; Mordecai, B. J.; Bhattacharjea, R.; Tong, W.; Wagner, B. K.; Flicker, J. D.; Turano, S. P.; Ready, W. J. *JOM* **2007**, *59*, 39−42.

(9) Leung, S.-F.; Gu, L.; Zhang, Q.; Tsui, K.-H.; Shieh, J.-M.; Shen, C.-H.; Hsiao, T.-H.; Hsu, C.-H.; Lu, L.; Li, D.; Lin, Q.; Fan, Z. *Sci. Rep.* **2014**, *4*, 4243.

(10) Naughton, M. J.; Kempa, K.; Ren, Z. F.; Gao, Y.; Rybczynski, J.; Argenti, N.; Gao, W.; Wang, Y.; Peng, Y.; Naughton, J. R.; McMahon, G.; Paudel, T.; Lan, Y. C.; Burns, M. J.; Shepard, A.; Clary, M.; Ballif, C.; Haug, F.-J.; Söderström, T.; Cubero, O.; Eminian, C. *Phys. Status Solidi RRL* **2010**, *4*, 181−183.

(11) Ramadurgam, S.; Lin, T.-G.; Yang, C. *Nano Lett.* **2014**, *14*, 4517−4522.

(12) Yu, R.; Ching, K.-L.; Lin, Q.; Leung, S.-F.; Arcrossito, D.; Fan, Z. *ACS Nano* **2011**, *5* (11), 9291−9298.

(13) Rizal, B.; Merlo, J. M.; Burns, M. J.; Chiles, T. C.; Naughton, M. J. *Analyst* **2015**, *140*, 39−58.

(14) Chan, K. T.; Kan, J. J.; Doran, C.; Ouyang, L.; Smith, D. J.; Fullerton, E. E. *Nano Lett.* **2010**, *10*, 5070−5075.

(15) Kim, S.-I.; Yoon, H.; Lee, H.; Lee, S.; Jo, Y.; Lee, S.; Choo, J.; Kim, B. *J. Mater. Chem. C* **2015**, *3*, 100−106.

(16) Kempa, K.; Rybczynski, J.; Huang, Z.; Gregorczyk, K.; Vidan, A.; Kimball, B.; Carlson, J.; Benham, G.; Wang, Y.; Herczynski, A.; Ren, Z. F. *Adv. Mater.* **2007**, *19*, 421−426.

(17) Zhang, L.; Austin, D.; Merkulov, V. I.; Meleshko, A. V.; Klein, K. L.; Guillorn, M. A.; Lowndes, D. H.; Simpson, M. L. *Appl. Phys. Lett.* **2004**, *84*, 3972−3974.

(18) Pawlek, F.; Rogalla, D. *Cryogenics* **1966**, *6*, 14−20.

(19) Asoh, H.; Nishio, K.; Nakao, M.; Tamamura, T.; Masuda, H. *J. Electrochem. Soc.* **2001**, *148*, B152−B156.

(20) Leung, S.-F.; Yu, M.; Lin, Q.; Kwon, K.; Ching, K.-L.; Gu, L.; Yu, K.; Fan, Z. *Nano Lett.* **2012**, *12*, 3682−3689.

(21) Stępniowski, W. J.; Salerno, M. Fabrication of nanowires and nanotubes by anodic alumina template-assisted electrodeposition. In *Manufacturing Nanostructures*; Ahmed, W., Ali, N., Eds.; One Central Press: Manchester, U.K., 2014; pp 321−357.

(22) Choi, J.; Sauer, G.; Nielsch, K.; Wehrspohn, R. B.; Gösele, U. *Chem. Mater.* **2003**, *15*, 776−779.

(23) Passi, V.; Dubois, E.; Lecestre, A.; Linde, A. S.; Bois, B. D.; Raskin, J.-P. *Microelectron. Eng.* **2013**, *103*, 57−65.

(24) Sun, Z.; Wang, D.; Xiang, J. *ACS Nano* **2014**, *8*, 11261−11267.

(25) Lee, M. H.; Lim, N.; Ruebusch, D. J.; Jamshidi, A.; Kapadia, R.; Lee, R.; Seok, T. J.; Takei, K.; Cho, K. Y.; Fan, Z.; Jang, H.; Wu, M.; Cho, G.; Javey, A. *Nano Lett.* **2011**, *11*, 3425−3430.

(26) Haxel, G. B.; Hendrick, J. B.; Orris, G. J.; Stauffer, P. H.; Hendley II, J. W.; *Rare Earth Elements−Critical Resources for High Technology*; Technical Report for U.S. Geological Survey: Reston, VA, 2002.

(27) Masuda, H.; Yamada, H.; Satoh, M.; Asoh, H.; Nakao, M.; Tamamura, T. *Appl. Phys. Lett.* **1997**, *71*, 2770−2772.

(28) Lee, W.; Park, S.-J. *Chem. Rev.* **2014**, *114*, 7487−7556.

(29) Masuda, H.; Yotsuya, M.; Asano, M.; Nishio, K.; Nakao, M.; Yokoo, A.; Tamamura, T. *Appl. Phys. Lett.* **2001**, *78*, 826−828.

(30) Smith, J. T.; Hang, Q.; Franklin, A. D.; Janes, D. B.; Sands, T. D. *Appl. Phys. Lett.* **2008**, *93*, 043108.

(31) Thompson, G. E.; Wood, G. C. *Nature* **1981**, *290*, 230−232.

(32) Yahalom, J.; Hoar, T. P. *Electrochim. Acta* **1970**, *15*, 877−884.

(33) Sato, N. *Electrochim. Acta* **1971**, *16*, 1683−1692.

(34) Garcia-Vergara, S. J.; Skeldon, P.; Thompson, G. E.; Habazaki, H. *Electrochim. Acta* **2006**, *52*, 681−687.

(35) Garcia-Vergara, S. J.; Hashimoto, T.; Skeldon, P.; Thompson, G. E.; Habazaki, H. *Electrochim. Acta* **2009**, *54*, 3662−3670.

(36) Baron-Wiecheć, A.; Burke, M. G.; Hashimoto, T.; Liu, H.; Skeldon, P.; Thompson, G. E.; Habazaki, H.; Ganem, J.-J.; Vickridge, I. C. *Electrochim. Acta* **2013**, *113*, 302−312.

(37) Vojkuvka, L.; Santos, A.; Pallarès, J.; Ferré-Borrull, J.; Marsal, L. F.; Celis, J. P. *Surf. Coat. Technol.* **2012**, *206*, 2115−2124.

(38) Nagpal, P.; Lindquist, N. C.; Oh, S.-H.; Norris, D. J. *Science* **2009**, *325*, 594−597.

(39) Ditlbacher, H.; Hohenau, A.; Wagner, D.; Kreibig, U.; Rogers, M.; Hofer, F.; Aussenegg, F. R.; Krenn, J. R. *Phys. Rev. Lett.* **2005**, *95*, 257403.

(40) Knight, M. W.; King, N. S.; Liu, L.; Everitt, H. O.; Nordlander, P.; Halas, N. J. *ACS Nano* **2014**, *8*, 834−840.

(41) Smith, D. Y.; Shiles, E.; Inokuti, M. The Optical Properties of Metallic Aluminum. In *Handbook of Optical Constants of Solids*; Palik, E. D., Eds.; Academic Press, Inc.: San Diego, CA, 1997; Vol. *1*, pp 369−406.

(42) Ekinci, Y.; Solak, H. H.; Löffler, J. F. *J. Appl. Phys.* **2008**, *104*, 083107.

(43) Martin, J.; Plain, J. *J. Phys. D: Appl. Phys.* **2015**, *48*, 184002.

(44) Zeman, E. J.; Schatz, G. C. *J. Phys. Chem.* **1987**, *91*, 634−643.

(45) Zorić, I.; Zäch, M.; Kasemo, B.; Langhammer, C. *ACS Nano* **2011**, *5*, 2535−2546.

(46) Kumar, P. S.; Pastoriza-Santos, I.; Rodríguez-González, B.; García de Abajo, F. J.; Liz-Marzán, L. M. *Nanotechnology* **2008**, *19*, 015606.

(47) Knight, M. W.; Liu, L.; Wang, Y.; Brown, L.; Mukherjee, S.; King, N. S.; Everitt, H. O.; Nordlander, P.; Halas, N. J. *Nano Lett.* **2012**, *12*, 6000−6004.

(48) Villesen, T. F.; Uhrenfeldt, C.; Johansen, B.; Hansen, J. L.; Ulriksen, H. U.; Larsen, A. N. *Nanotechnology* **2012**, *23*, 085202.

(49) Horcas, I.; Fernández, R.; Gómez-Rodríguez, J. M.; Colchero, J.; Gómez-Herrero, J.; Baro, A. M. *Rev. Sci. Instrum.* **2007**, *78*, 013705.

Supporting Information for nl-2015-02408w

Aluminum Nanowire Arrays via Directed Assembly

Nathan T. Nesbitt,* Juan M. Merlo, Aaron H. Rose, Yitzi M. Calm, Krzysztof Kempa, Michael J. Burns, and Michael J. Naughton*

Department of Physics, Boston College, 140 Commonwealth Avenue, Chestnut Hill, MA 02467

Experimental methods for Al nanowire array fabrication

Here, Ni posts were used to imprint the Al surface with an array of indents. Ni was chosen because of its hardness and compatibility with an electron-beam lithography (EBL) technique for fabricating post arrays. The use of EBL allowed Ni posts to be left out of certain lattice sites in the array, such that after imprinting the Al there would be missing indents at certain lattice sites of the indent array. This prevented the Al from anodizing at the sites of the missing indents. As shown in Figure S1, there is apparently a maximum indent diameter for which pores selectively nucleate at indented sites and not sites missing an indent. Figure S2 shows photographs of the experimental setup used in the fabrication of Ni posts and Al nanowires.

Stamp preparation: To produce the stamp in Figure 2a, glass slides 16 mm x 15 mm were piranha cleaned and then coated with 50 nm of Ni with a Sharon electron beam deposition

system. HMDS (VLSI grade 0.1 μm filtered from Ultra Pure Solutions, Inc.) was spun on (step 1: 5 sec, 500 rpm, 100 rpm/sec; step 2: 45 s, 4000 rpm, 550 rpm/s) to remove moisture from the sample surface, followed by electron beam resist (950 PMMA A4 from MicroChem) spun on (step 1: 5 s, 500 rpm, 100 rpm/s; step 2: 45 s, 4000 rpm, 550 rpm/s) to create a nominally 200 nm thick PMMA film. A 120 s delay between applying the PMMA and initiating the spin steps was included to allow bubbles in the PMMA to dissipate. The PMMA was then pre-expose baked at 180 ºC for 25 min on a hotplate. Arrays of nominally 100 nm diameter holes were written into the PMMA with a JEOL SEM using a dosage of ~ 1300 μC/cm^2. The PMMA was then developed with 1:3 MicroChem MIBK:IPA (MIBK/IPA 1:3 Developer from MicroChem) for 40 s, IPA for 20 s, and finally de-ionized water (DI) for 20 s. Ni was then electroplated into the holes using Ni plating solution (SN-10 Ni Plating Solution from Transene, Inc.), a counter electrode (47 mm^2 of exposed surface area of coil of Pt wire, 0.1 mm diameter, Premion 99.997% Pt from Alfa Aesar), and a potentiostat (Gamry Interface 1000 running a chronopotentiometry scan) to produce nominally 100 nm tall Ni posts. The PMMA was subsequently dissolved by placing the stamp in a bath of acetone for a few minutes.

Electropolish Al: High purity Al foil (annealed, Puratronic, 99.9995%, Alfa Aesar) of thickness 200 μm and surface roughness of 30 nm (measured by AFM), was cut into 5 mm x 10 mm strips using scissors. The strips were flattened between two glass slides using a custom-made vice composed of two flat Al plates (one plate could move vertically by turning a 5 mm diameter screw, the other comprised the base of the vice). The Al foil was then rinsed with ethanol to remove moisture from the surface (moisture causes degradation of the Al surface during electropolishing – specifically the appearance of a rough off-white film) and immersed in a bath of 1 perchloric acid : 3 ethanol (70% perchloric acid Reagent ACS Grade from GFS

Chemicals, 90% ethanol (5.5% Isopropanol, 4.5% Methanol) HPLC Grade from Fisher), which was stirred at 120 rpm with a 10 mm magnetic Teflon coated stirring rod and held at 5 ºC via a jacketed beaker and circulating bath (Polystat 1212202 from Cole Parmer). A 5 mm diameter 80 mm length carbon rod (Fisher Scientific, cat. no. S43501) was simultaneously immersed in the solution as a counter electrode. Electrical contact was made to the Al foil and C rod via flat-tipped alligator clips (Micro 1-1/8" Smooth Clips from RadioShack). 10-20 V was applied with a high current voltage source (Kepco model: KS36-10M current regulated power supply) for 5-10 min (voltage and time were fine-tuned each day electropolishing took place). The polished Al had a mirror finish with surface roughness 3.9 nm as determined by AFM.

Imprint Al: The polished Al foil was placed polished-side-down on top of the Ni stamp (with Ni posts facing up) and a small piece (2 mm x 2 mm) of Teflon plumbing tape was placed on top of the Al at the region to be imprinted. This stack was sandwiched between two glass slides, and the sandwich was placed into the custom vice. The vice was carefully closed to compress the Al against the Ni stamp and imprint the Al. The imprinted Al developed iridescence in the region imprinted by Ni posts, and had a surface roughness of 2.8 nm.

Anodize Al: A 2.5-3.5 mm diameter circular window was cut into adhesive Teflon tape (Tape with PTFE Film, Beige 5498, Silicon-free, 4 mil, part #5498-10 from All-Spec Industries), and the tape was used to mask the imprinted Al foil. The tape was arranged such that the window exposed the imprinted region of the Al. The Al foil was placed in a beaker of:

50 ml Ethylene Glycol (E178-4 Ethylene Glycol Certified from Fisher)

50 ml 2%wt Citric acid (anhydrous, reagent ACS, 99.5% from Acros in DI)

2.9 ml 0.1%wt Phosphoric acid (85% solution from Acros Organics in DI)

which was held at 10 ºC via a jacketed beaker and circulating bath (Polystat 1212202 from Cole Parmer). For Al nanowires with a minimum pitch of 2.4 μm (*i.e.* an AAO template of pitch 1.2 μm), 480 V was applied with a DC voltage source (Fluke 412B) between the Al foil and a carbon counter electrode for a duration appropriate for the desired height of the Al nanowires.

Etch Al$_2$O$_3$: The anodized Al foil was rinsed with DI and placed for 50 minutes in a beaker containing 50 ml of 6%wt Phosphoric Acid (85% Phosphoric acid from Acros Organics) and 1.8%wt Chromic Acid (10% w/v Chromic Acid from Ricca Chemical Company) in DI held at 63 ºC.

Final Rinse: The Al foil was rinsed with DI and dried by flowing a nitrogen stream across it. This exposed the Al nanowires allowing them to be imaged via SEM. Iridescence was visible to the eye where there were Al nanowires.

Table S1. Trends in AAO fabrication procedures, organized by anodization solution, including the impact that a missing indent has on pore formation.

| Anodization solution:	Oxalic acid	Phosphoric acid	Citric + phosphoric + EG
Anodization voltage:	80 V (ref 1)	120 V (ref 2)	480 V (this work)
Pitch of pores in AAO template:	200 nm (ref 1)	300 nm (ref 2)	1200 nm (this work)
Percent of barrier oxide at pore base penetrated by anions:	90% (ref 3)	66% (ref 3)	No data
Pore formation at missing indent:	Nearly normal pore (ref 1)	Small pore with diamond shaped adjacent pores (ref 2)	Pore formation blocked to produce Al nanowire (this work)
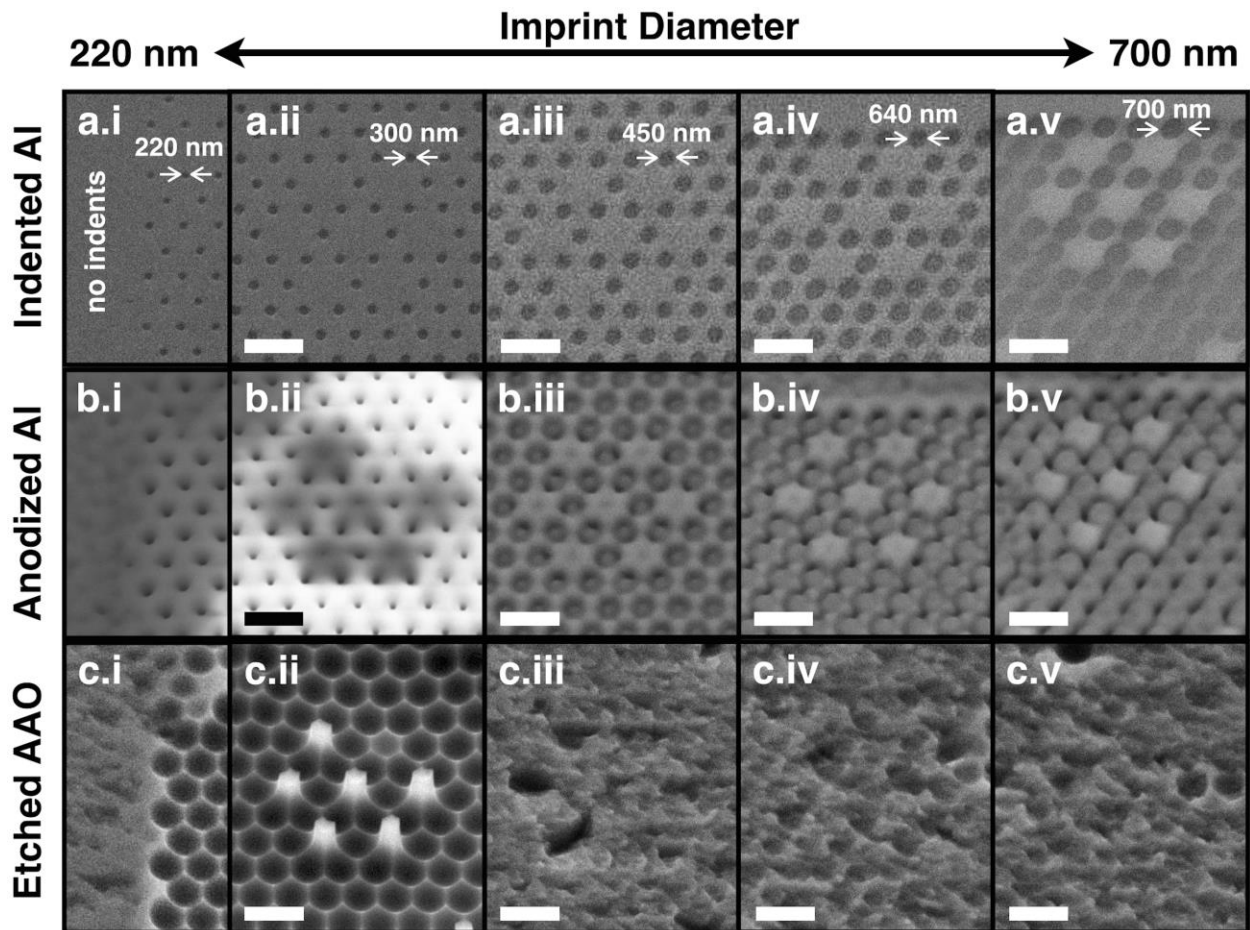
Figure S1. SEM images showing the dependence of Al nanowire growth on imprint post diameter. Images show fabrication steps: (a) imprinted Al, (b) anodized Al, (c) Al surface after etching away anodized aluminum oxide. These images, along with the results in Figure 3, show that: (i) pores did not nucleate in the area on the left with no indents, (ii) indents of diameter $\leq$ 400 nm produced pores at indent sites and Al nanowires at missing indent sites, (iii-v) indents of diameter > 450 nm did not cause pores to nucleate. At areas where no pores nucleated, the anodized aluminum oxide was approximately conformal to the Al surface; after etching this oxide away a rough and planar Al surface was revealed. Thus, for an indent array pitch of 1.2 μm, this sample suggests imprint post diameter must be $\leq$ 400 nm for an AAO template and

embedded Al nanowires to form. SEMs (a.i) and (a.ii) are representative images from areas of the sample neighboring (b.i), (c.i) and (b.ii), (c.ii), respectively. Scale bars 2 μm.
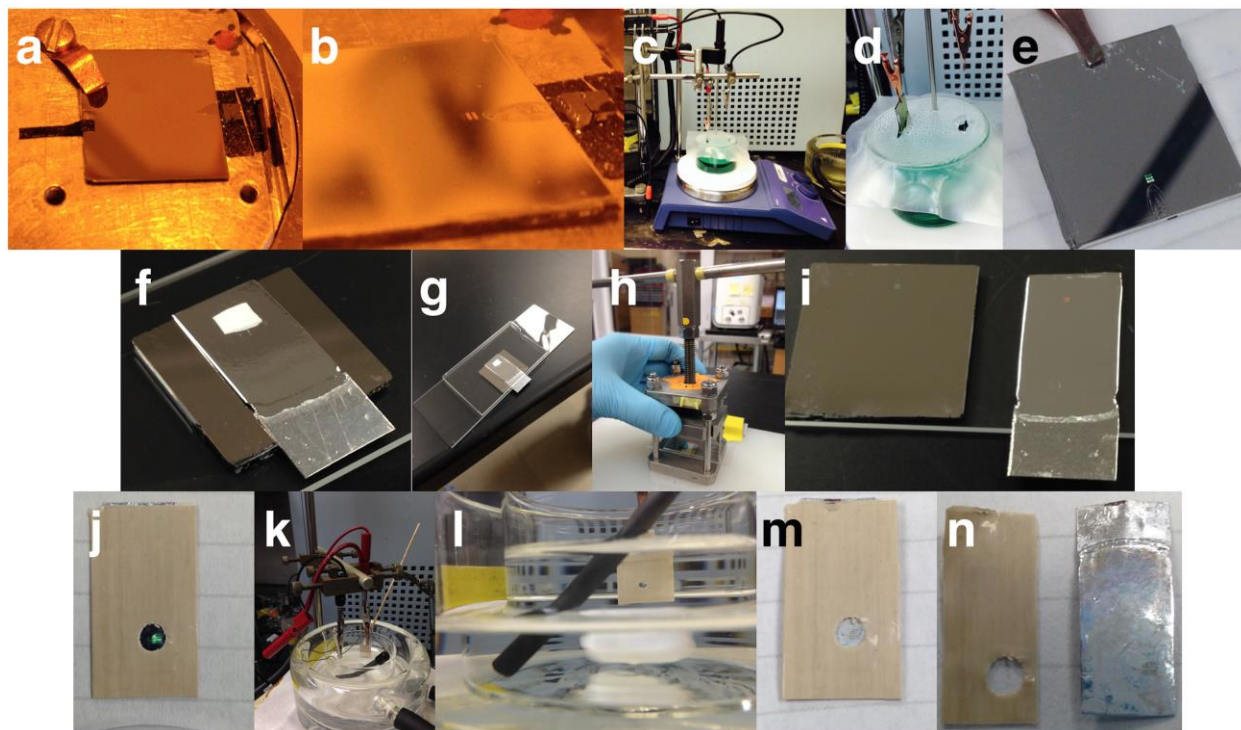
Figure S2. Photos of fabrication process and setup: (a) Ni-coated glass with PMMA film for EBL, (b) after development of the nanopores in the PMMA film, (c-e) electrodeposition of Ni into the PMMA pores, (f) stack of electropolished Al lying polished side-down on Ni posts, with PTFE tape over region to be stamped, (g) stack sandwiched between two glass slides, (h) custom-made vice for indenting the Al, (i) Ni stamp and the indented Al, (j) Al masked with adhesive PTFE tape, with a window exposing the indented region of the Al, (k) anodization setup including the jacketed beaker for temperature control, (l) carbon rod counter electrode, PTFE coated magnetic stirring rod, and masked Al during anodization, (m) Al after anodization, (n) Al and PTFE tape after removal of the tape.
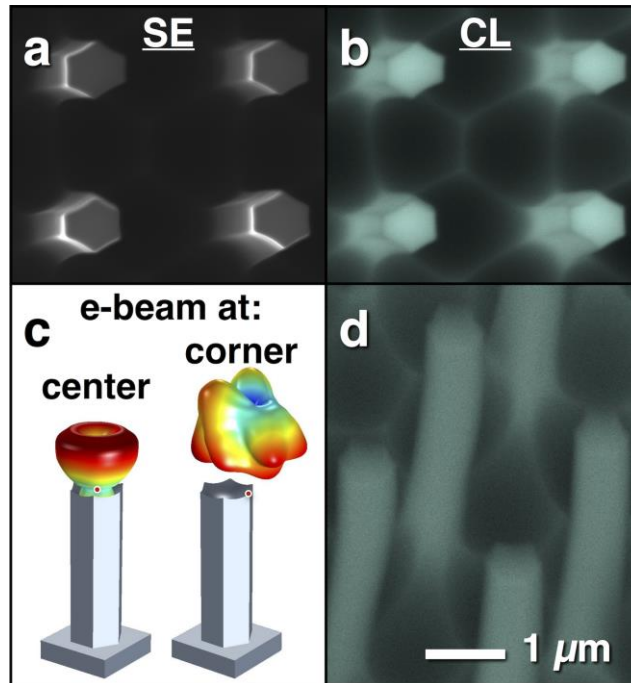
Figure S3. SEM, panchromatic cathodoluminescence, and simulations of Al nanowire arrays. (a) Secondary electron (SE) image of an Al nanowire array (sample tilt 0º). (b) Panchromatic cathodoluminescence (CL) image (350-650 nm) of an Al nanowire array (sample tilt 0º) showing dark highlights at the sharp edges of the nanowires. (d) CL image of an Al nanowire array (sample tilt 30º) showing light highlights at sharp edges of the nanowires. (c) Simulations of the radiation pattern for two cases: electric dipole (with vertical moment) excitation at the center (left) and at the corner (right) of the nanowire top, represented by a red dot. The radiation pattern is expected to represent the cathodoluminescent response of the nanowire to excitation by the electron beam. For the dipole at the nanowire top-center, the radiation pattern has maxima directed upwards away from the nanowire, with a broad minima in the plane perpendicular to the nanowire. For the dipole at the corner, the radiation pattern shows maxima in the plane perpendicular to the wire axis, and a broad minima upwards away from the nanowire. This is consistent with the dark and bright highlights observed by CL at the sharps edges relative to the top face of the nanowires for 0º and 30º sample tilts.
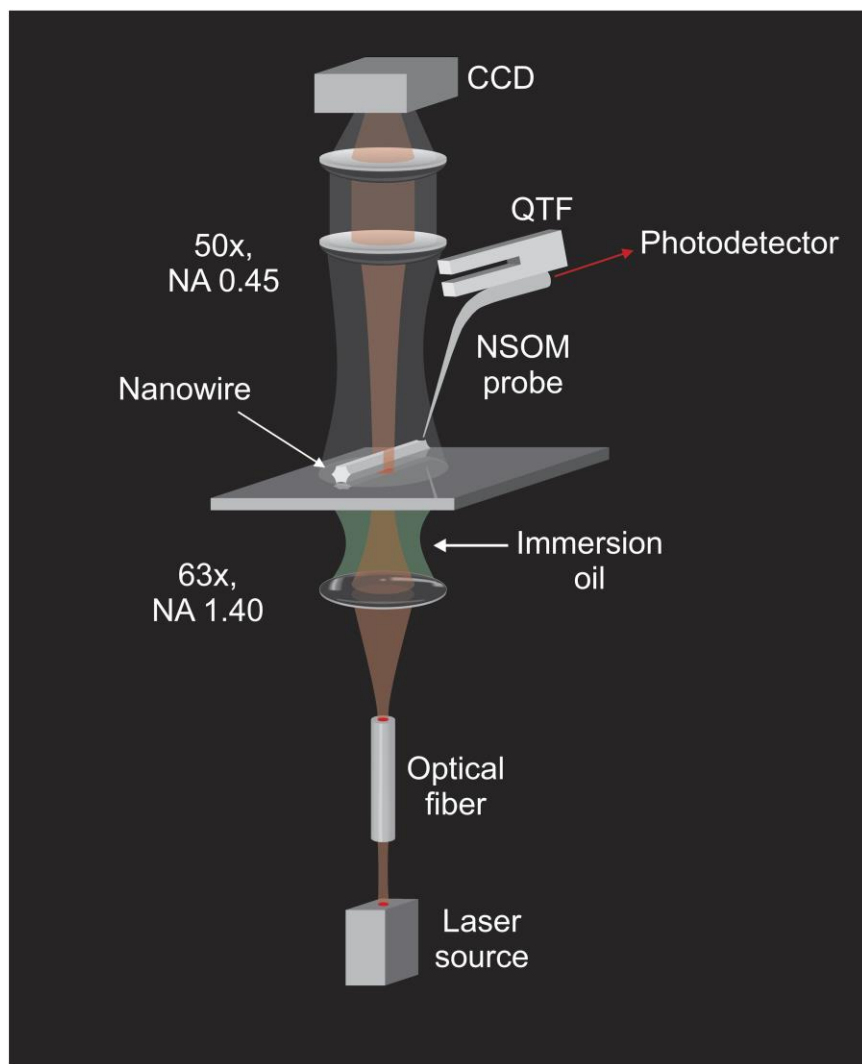
Figure S4. Schematic of experimental setup for NSOM measurements of an Al nanowire. A Nanonics Imaging Ltd. MultiView 4000 NSOM was used to illuminate the nanowire with a 660 nm wavelength laser source. A single-mode optical fiber, diameter 4 μm, coupled light from the laser into a 63× numerical aperture (NA) = 1.40 objective below the Al nanowire. Laser light passed from this objective, through immersion oil and a glass slide to form a spot in a focal plane containing the Al nanowire. Far-field radiation from the laser spot was observed by a charge-coupled device (CCD) camera through a 50× NA=0.45 objective above the nanowire. Near-field radiation at the nanowire and glass surfaces was measured by an NSOM probe (100 nm aperture, 150 nm Cr-Au coating, multimode fiber).

REFERENCES

(1)   Masuda, H.; Yotsuya, M.; Asano, M.; Nishio, K.; Nakao, M.; Yokoo, A.; Tamamura, T. *Appl. Phys. Lett.* **2001**, 78, 826–828.

(2)   Smith, J. T.; Hang, Q.; Franklin, A. D.; Janes, D. B.; Sands, T. D. *Appl. Phys. Lett.* **2008**, 93, 043108.

(3)   Thompson, G. E.; Wood, G. C. *Nature* **1981**, 290, 230–232.